

# Template-derived high surface area $\lambda$ -MnO<sub>2</sub> for supercapacitor applications

Camelia Matei Ghimbeu · Agnieszka Malak-Polaczyk ·  
Elzbieta Frackowiak · Cathie Vix-Guterl

Received: 30 April 2013 / Accepted: 10 August 2013 / Published online: 28 August 2013  
© Springer Science+Business Media Dordrecht 2013

**Abstract** The synthesis of lambda-manganese oxide ( $\lambda$ -MnO<sub>2</sub>) with a developed porosity and an ordered and interconnected pore structure used as supercapacitor electrode is reported for the first time in the present study. A spinel-type LiMn<sub>2</sub>O<sub>4</sub> material was first prepared by hard-templating pathway using KIT-6 mesoporous silica as a template and metal nitrates as precursors, which was subsequently acid treated leading to  $\lambda$ -MnO<sub>2</sub> material. The materials exhibit high surface area (up to 150 m<sup>2</sup> g<sup>-1</sup>), defined pore size distribution with three-dimensional interconnected pores, and crystalline pore walls. The material textural properties as well as the morphologies vary considerably with the synthetic conditions. The as-synthesized porous  $\lambda$ -MnO<sub>2</sub> materials exhibit a noticeably better performance (120 F g<sup>-1</sup>) at high constant currents (1 A g<sup>-1</sup>) than commercial derived  $\lambda$ -MnO<sub>2</sub> (11 F g<sup>-1</sup>). The extended surface area and the porous and three-dimensional interconnected structures along with the specific morphology significantly enhance the lithium diffusion through the particles and allow for a more effective use of this pseudocapacitive material as an electrode in supercapacitor.

**Keywords** Lambda-manganese oxide · Pseudocapacitance · Supercapacitor · Template

## 1 Introduction

Supercapacitors are attractive energy storage systems, which supply or collect the charge in a very short time and exhibit high power and long durability [1]. Among the materials employed as electrodes for supercapacitors, the manganese oxide is the most studied one because of its major advantages, i.e., high theoretical capacity, low cost, and environmental-friendly nature [2, 3]. Although many MnO<sub>2</sub> crystalline phases were evaluated as electrodes [4, 5], the lambda-manganese oxide ( $\lambda$ -MnO<sub>2</sub>) was only recently proposed as suitable electrode for supercapacitors [6, 7].

The literature concerning the synthesis of  $\lambda$ -MnO<sub>2</sub> is scarce, and to our knowledge, the only existing method is based on the delithiation of LiMn<sub>2</sub>O<sub>4</sub> spinel [8]. In this process, the lithium ions can be extracted from spinel, and at the same time, LiMn<sub>2</sub>O<sub>4</sub> undergoes conversion to the defected MnO<sub>2</sub> phase, while preserving the spinel structural framework of the LiMn<sub>2</sub>O<sub>4</sub>. The Li-ion extraction can be carried out either by an electrochemical or chemical method. In the case of the electrochemical process, the Li ions are removed by applying an electrical current between a LiMn<sub>2</sub>O<sub>4</sub> electrode and a counter electrode that acts as a Li sink [2, 3]. This process is analogous to the charging of Li-ion battery. Chemical delithiation involves the dissolution of lithium oxide and surface disproportionation reaction of two trivalent manganese ions in the presence of an acid. Despite having the same structure,  $\lambda$ -MnO<sub>2</sub> obtained by electrochemical process may differ from the product of chemical extraction because insertion of additional proton can occur in acidic solution [9].

In our previous study [6], the  $\lambda$ -MnO<sub>2</sub> material was obtained by chemical delithiation of a commercial LiMn<sub>2</sub>O<sub>4</sub> in sulfuric acid solutions. Despite the advantages

C. Matei Ghimbeu (✉) · A. Malak-Polaczyk · C. Vix-Guterl  
Institut de Science des Matériaux de Mulhouse, CNRS UMR  
7361, 15 Rue Starcky, 68057 Mulhouse, France  
e-mail: camelia.ghimbeu@uha.fr

A. Malak-Polaczyk · E. Frackowiak  
Institute of Chemistry and Technical Electrochemistry, Poznan  
University of Technology, Piotrowo 3, 60-695 Poznan, Poland

of this material (high capacitance and energy density), a significant decrease of the specific capacitance values at high current densities was observed [6]. This can be probably related to several factors such as conductivity, particle size and geometry, crystallinity, surface area, etc. Furthermore, the commercial derived  $\lambda$ - $\text{MnO}_2$  used exhibited a too low specific surface area ( $5 \text{ m}^2 \text{ g}^{-1}$ ), and in this case, the utilization of this type of pseudocapacitive material for the ion insertion is limited only to the outer surface of the electrode. Hence, an enhancement of the electrochemical performance could be expected through a significant increase of the surface area of the electrode material. The developed porosity could then favor the diffusion of the lithium through the particles [10] and permit a more effective utilization of the pseudocapacitive material as an electrode in the supercapacitor.

Therefore, the development of new synthesis pathways leading to  $\lambda$ - $\text{MnO}_2$  material with tailored characteristics (high surface area, controlled pore size distribution, etc.) is highly required. However, since the starting material to prepare  $\lambda$ - $\text{MnO}_2$  is  $\text{LiMn}_2\text{O}_4$ , a well-known cathode material for lithium-ion batteries [11–15], little attention was paid to synthesize it with high surface area [2, 3, 10].

The use of  $\text{LiMn}_2\text{O}_4$  as an electrode in a hybrid supercapacitor was recently mentioned in the literature [16, 17,] but we showed that  $\lambda$ - $\text{MnO}_2$  is a more interesting material to be used as supercapacitor electrode, since it exhibits better electrochemical performance [6, 7]. Moreover, the combination of  $\lambda$ - $\text{MnO}_2$  as the positive electrode and activated carbon used as the negative electrode led to an asymmetric capacitor that can work in an extended potential window up to 2.5 V [6].

Among the possibilities to synthesize high-surface area  $\text{LiMn}_2\text{O}_4$  and  $\lambda$ - $\text{MnO}_2$ , the hard-template synthesis process appears as an efficient procedure, successfully applied for the preparation of other inorganic compounds [18–26]. In particular,  $\text{LiMn}_2\text{O}_4$  and  $\text{LiCoO}_2$  were synthesized by this approach [10]. The synthesis involved two steps: first, the preparation of mesoporous  $\text{Mn}_2\text{O}_3$  ( $\text{Co}_3\text{O}_4$ ) by impregnation of the template with a metal precursor solution followed by thermal treatment and template removal, while in a second step  $\text{Mn}_2\text{O}_3$  ( $\text{Co}_3\text{O}_4$ ) reacted with a lithium source ( $\text{LiOH}$ ) to form the corresponding lithium-containing oxide.

Ordered mesoporous silica (i.e., SBA15, KIT-6...), and ordered porous carbons or activated carbons are currently employed as hard templates. The ordered porous silica and carbons are advantageous over activated carbons as they have uniform pore size distribution, high surface area, and interconnected pores that are suitable characteristics for improved ionic transport and improved power density. In addition, since the final product corresponds to the negative replica of the template, selecting the suitable template can

control its texture. In this manner, the adjustment of the porosity to the size of the electrolyte ions becomes possible [27–30].

Taking above mentioned advantages into account, we report here on the synthesis of  $\lambda$ - $\text{MnO}_2$  material with a high surface area by using a templating process. A mesoporous silica (KIT-6) was selected as hard template, and the Li and Mn metal nitrates precursors were simultaneously infiltrated into silica porosity, the template removed to obtain  $\text{LiMn}_2\text{O}_4$ , and further acid treatment allowed porous ordered  $\lambda$ - $\text{MnO}_2$  to be formed. The materials were physically characterized, and the physicochemical properties were correlated with the electrochemical measurements performed in a two-electrode cell containing  $\text{Li}_2\text{SO}_4$  aqueous environmentally friendly electrolyte.

## 2 Experimental section

### 2.1 Material preparation

Powdered lithium-manganese oxide ( $\text{LiMn}_2\text{O}_4$ ) was supplied by MERCK [lithium manganese (III, IV) oxide cathode powder]. Sulfuric acid (95 %), lithium sulfate, sodium hydroxide, lithium nitrate, and manganese nitrate, commercially available reagents (p.a.) were procured from Aldrich and Fluka. For the synthesis of porous  $\text{LiMn}_2\text{O}_4$ , mesoporous cubic silica KIT-6 was employed as hard template. The preparation of the template was performed according to a procedure reported by Ryoo and coworkers [31]. In brief, 6 g of triblock polymer pluryonic P123 was dissolved in a mixture of 217 g of distilled water and 11.8 g of concentrated HCl (35 %). Then, 6 g of butanol was added at 35 °C under stirring. After 1 h of stirring, 12.9 g of TEOS was added at 35 °C. After 24 h of stirring at 35 °C and subsequent hydrothermal treatment for 24 h at 100 °C under static conditions, the obtained solid product was filtered and dried at 100 °C without washing. The template was removed by chemical extraction in an ethanol–HCl mixture, followed by a thermal treatment at 550 °C. The as-prepared silica possesses a BET surface area of  $879 \text{ m}^2 \text{ g}^{-1}$  and a pore volume of  $1.3 \text{ cm}^3 \text{ g}^{-1}$ .

For a typical synthesis of oxides, metal nitrates ( $\text{LiNO}_3$  and  $\text{Mn}(\text{NO}_3)_2 \cdot 4\text{H}_2\text{O}$ ) were dissolved in ethanol with a Mn/Li molar ratio of 1:1. Template-derived materials were produced by filling the porous structure of the silica KIT-6 with a concentrated solution (4 M) of precursors until incipient wetness was attained (about 1 mL of liquid for 0.5 g silica) or a diluted solution of precursors (10 mL solution 0.3 M for 0.5 g silica).

The impregnated samples were then thermally treated in air at 600 °C ( $5 \text{ }^\circ\text{C min}^{-1}$ ) for 4 h. The silica framework was then completely removed with 2 M NaOH solution at

100 °C for 24 h. The resulting materials are denoted LiMn<sub>2</sub>O<sub>4</sub>-C and LiMn<sub>2</sub>O<sub>4</sub>-D for the spinels prepared with concentrated and diluted solutions, respectively.

Lithium extraction leading to the manganese dioxide compound was achieved by immersing the LiMn<sub>2</sub>O<sub>4</sub> powders in an aqueous solution of sulfuric acid (1 M) and by stirring the mixture for 4 h. Afterward, the solution was filtered, washed several times with distilled water, and dried in air at 100 °C. The final products are designated as λ-MnO<sub>2</sub>-C and λ-MnO<sub>2</sub>-D, which correspond to the starting LiMn<sub>2</sub>O<sub>4</sub> spinels. For comparison, commercial LiMn<sub>2</sub>O<sub>4</sub> was also treated by a similar aqueous sulfuric acid solution under the same conditions. The product of this material is denoted λ-MnO<sub>2</sub>.

## 2.2 Physical measurements

The morphologies of the samples were examined by scanning electron microscopy (Philips model FEI model Quanta 400) and transmission electron microscopy (Philips CM200). The textural properties of the materials were determined by nitrogen adsorption at 77 K using a Micromeritics ASAP 2020 apparatus. Before analysis, the materials were outgassed overnight under vacuum at 150 °C. The specific surface area was evaluated according to the BET equation in the 0.05–0.3 region of relative pressure. The total pore volume was determined at a relative pressure  $P/P_0 = 0.95$ , while the pore size distribution was calculated by the BJH method using the desorption branches.

The crystallinity and the structure of the samples were determined by X-ray diffraction technique. XRD analysis of each sample was carried out using Philips X'pert MPD diffractometer equipped with a Cu anode to generate CuKα radiation ( $\lambda = 1.5406 \text{ \AA}$ ). Each diffraction pattern was collected in the  $2\theta$  range 15–70° with the step size of 0.05° and a count time of 5.0 s per step.

## 2.3 Electrochemical characterizations

The capacitor electrodes for evaluating the electrochemical properties were formed as pellets consisting of 75 wt% active electrode material, 20 wt% acetylene black, and 5 wt% binder (PVDF, Kynar Flex 2801). These pellets were 10 mm in diameter and 0.20 mm ( $\pm 0.02 \text{ mm}$ ) in thickness and were prepared under pressure of 10 MPa. The typical mass of the electrode material ranged from 9.0 to 14.0 mg. Symmetric supercapacitors were operating in a 1 M Li<sub>2</sub>SO<sub>4</sub> electrolytic aqueous solution which is cheaper, safer, and more environmental friendly than the organic electrolytes. All the experiments were carried out at room temperature.

The capacitance values were estimated in a two-electrode Swagelok<sup>®</sup> cell system by galvanostatic charge/discharge,

impedance spectroscopy and cyclic voltammetry with different scan rates using a VMP3 (Bio-Logic) multichannel potentiostat. The capacitance values of the material were normalized to the mass of active material in one electrode. The specific capacitance has been evaluated using the formula  $C = I\Delta t/(m\Delta V)$ , where  $i$  is the current used for discharge,  $\Delta t$  is the time elapsed for the discharge,  $m$  is the mass of the active electrode, and  $\Delta V$  is the voltage range of the discharge. The impedance spectroscopy measurements were carried out in the range of frequencies from 1 mHz to 100 Hz with an excitation signal of 10 mV amplitude.

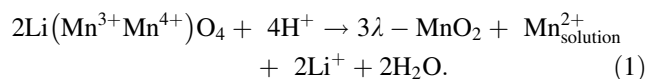
## 3 Results and discussion

The X-ray diffraction patterns of the templated as well as the commercial LiMn<sub>2</sub>O<sub>4</sub> before and after delithiation are reported in Fig. 1. This figure shows the formation of crystalline LiMn<sub>2</sub>O<sub>4</sub> for the synthesized and commercial samples. The peaks could be assigned to pure cubic spinel structure [Joint Committee for Powder Diffraction Studies (JCPDS) 35-0782]. No additional impurity peaks are detected.

Compared with the LiMn<sub>2</sub>O<sub>4</sub> synthesized by the templating process, the lattice parameter value is higher in the case of λ-MnO<sub>2</sub> derived from commercial LiMn<sub>2</sub>O<sub>4</sub> (Table 1). This can indicate a composition of the as-synthesized materials (Li<sub>1+x</sub>Mn<sub>2-x</sub>O<sub>4</sub>,  $0.1 < x < 0.3$ ) slightly different from the commercial one which is close to the stoichiometric LiMn<sub>2</sub>O<sub>4</sub>.

The corresponding λ-MnO<sub>2</sub> compounds (λ-MnO<sub>2</sub>, λ-MnO<sub>2</sub>-C, and λ-MnO<sub>2</sub>-D) display the same pattern concerning the relative line position, while the peaks slightly shift toward lower  $d$  values (higher  $2\theta$ , Table 1), and their intensity magnitudes slightly decrease. This indicates that the LiMn<sub>2</sub>O<sub>4</sub> spinel structure is maintained after removal of lithium ions but is accompanied by a decrease of the lattice parameter ( $a$ , Table 1) as already mentioned in the literature [10].

This is due to the decrease of the Mn–Mn and Mn–O bond lengths after the removal of Li and disproportionation of Mn<sup>3+</sup> [8, 9, 32]. Feng et al. [32] suggested that the delithiation occurs mainly through redox reactions involving dissolution of lithium oxide and surface disproportionation reaction of two trivalent manganese ions. The charge of extracted lithium ions can be compensated by a change in valence state of the manganese ions. Therefore, the following reaction was proposed by Hunter [8]:



It must be noted that the chemical formula of LiMn<sub>2</sub>O<sub>4</sub> can be written as Li(Mn<sup>3+</sup>Mn<sup>4+</sup>)O<sub>4</sub> [11]. In fact, LiMn<sub>2</sub>O<sub>4</sub>

spinel crystallizes in a cubic close-packed structure. One-eighth of the total tetrahedral sites of lattice are occupied by lithium ions, and one half of the total octahedral sites are occupied by manganese ions. Therefore, in stoichiometric spinel, the manganese ions coexist in two valence states  $\text{Mn}^{3+}$  and  $\text{Mn}^{4+}$  in equal proportions. After acidic treatment, most of the lithium ions are removed from the tetrahedral sites, and the structural framework of spinel is preserved thereby decreasing the lattice parameter. All values are in good agreement with the reported data for pure phase of  $\lambda\text{-MnO}_2$  (JCPDS no 44-0992).

Nevertheless, some other differences can clearly be noticed between the synthesized materials and the commercial one. Compared with the  $\lambda\text{-MnO}_2$  obtained from commercial  $\text{LiMn}_2\text{O}_4$  (Fig. 1a), the peaks of the replicated oxides  $\lambda\text{-MnO}_2\text{-C}$  and  $\lambda\text{-MnO}_2\text{-D}$  (Fig. 1b, c) display a lower intensity and a larger width suggesting a smaller particles size and/or lower crystallinity. The mean crystallites sizes ( $L$ ) calculated with Scherrer formula [33] are listed in Table 1. The crystallites size of commercial  $\lambda\text{-MnO}_2$  is about 28 nm, while that of the synthesized  $\lambda\text{-MnO}_2\text{-C}$  and  $\lambda\text{-MnO}_2\text{-D}$  is indeed smaller, i.e., 17 and 19 nm, respectively. This size is almost the same as before delithiation for the porous materials ( $\text{LiMn}_2\text{O}_4\text{-C}$ , and  $\text{LiMn}_2\text{O}_4\text{-D}$ ). In the case of commercial  $\text{LiMn}_2\text{O}_4$ , a significant decrease in the crystallite size is, however, noticed after lithium extraction (35.6–28 nm).

The morphologies of the commercial and synthesized  $\text{LiMn}_2\text{O}_4$ , which were analyzed by SEM and TEM, are presented in Fig. 2a–d. In Fig. 2a, the SEM pictures of commercial  $\text{LiMn}_2\text{O}_4$  at low magnification show spherical particles with sizes in the range of 5–30  $\mu\text{m}$ . At high magnifications as presented in Fig. 2b, a dense morphology with embedded particles of approximately 0.5  $\mu\text{m}$  is observed. The synthesized materials, as illustrated in Fig. 2c, d, exhibit a porous morphology with small spherical particle sizes (<1  $\mu\text{m}$ ) which is in good agreement with oxides replicated with silica KIT-6 [34]. By comparing Fig. 2c with 2d, we observe that the particle size is larger for the sample obtained with concentrated solutions than the ones obtained with diluted solutions.

Details about the particles' morphologies of the  $\lambda\text{-MnO}_2\text{-C}$ ,  $\lambda\text{-MnO}_2\text{-D}$ , and silica KIT-6 on a nanometer scale are assessed by TEM and are shown in Fig. 3a, b, 3c, d, and 3e, f, respectively. A difference in the morphologies of the particles depending on the preparation conditions is observed. Magnification of the particles obtained by filling the silica with concentrated solution of precursors as shown in Fig. 3a, b, consists of entangled nanorods gathered in spherical particle geometry. Figure 3c, d reveals the ordered pore structure of the  $\lambda\text{-MnO}_2\text{-D}$  manganese oxide prepared with dilute precursor solution. This structure is replicating the porous structure of the three-dimensional

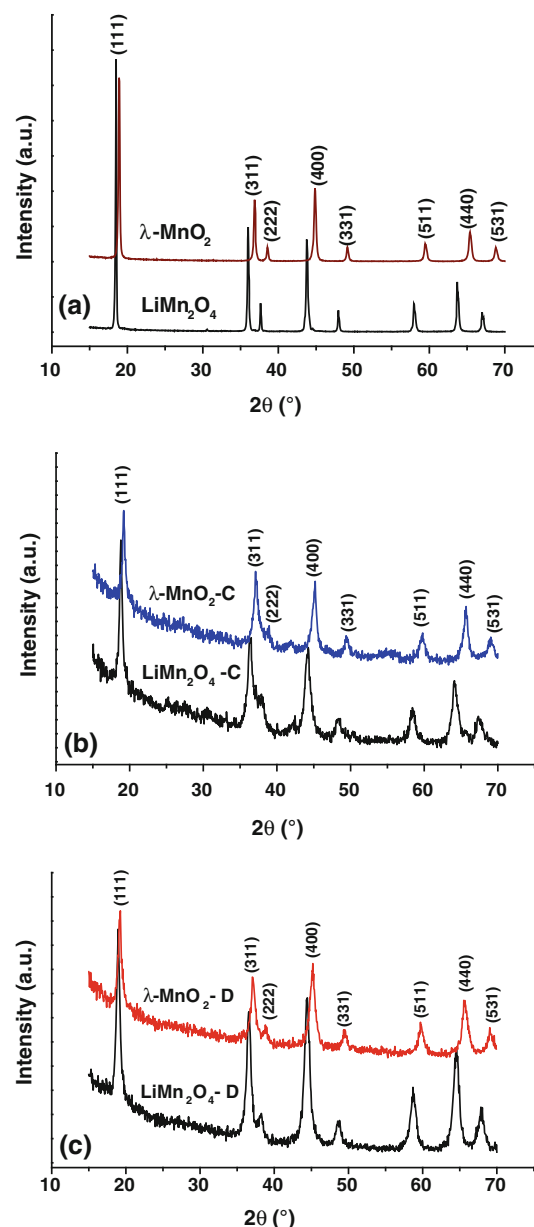


**Fig. 1** XRD patterns of commercial **a**  $\text{LiMn}_2\text{O}_4$ , **b**  $\text{LiMn}_2\text{O}_4\text{-C}$  and **c**  $\text{LiMn}_2\text{O}_4\text{-D}$  and their corresponding  $\lambda\text{-MnO}_2$

silica KIT-6 host as presented in Fig. 3e, f but with a lower degree of ordering. The particle sizes ranges are between 400 and 800 nm for  $\lambda\text{-MnO}_2\text{-C}$ , and 600 nm and 1.2  $\mu\text{m}$  for  $\lambda\text{-MnO}_2$ .

In order to verify the effectiveness of the applied synthesis pathway of increasing the specific surface area, nitrogen sorption measurements were carried out, and the results are presented in Fig. 4. All the isotherms show the same shape and can be categorized to the type IV, which is characteristic of mesoporous materials [35]. The appearance of hysteresis loops for all isotherms, which are associated with capillary condensation in mesopores, reveals a



certain degree of mesoporosity. The hysteresis loop is of type H4 and related to slit-shaped pores. The calculated values of the specific surface area and total pore volume are listed in Table 1. The data indicate that the use of a template allows the synthesis of high surface area  $\lambda$ -MnO<sub>2</sub> with a well-defined pore size. As for the morphology, it can be observed that the characteristics vary with the synthetic conditions especially with the concentration of the precursor solution. The highest specific surface area of 123 m<sup>2</sup> g<sup>-1</sup> was observed for the LiMn<sub>2</sub>O<sub>4</sub>-C sample where the concentration of the precursor was high.

The formation of mesopores is clearly visible on the pore size distribution curves presented in the inset of Fig. 3. The pore sizes of LiMn<sub>2</sub>O<sub>4</sub>-C and LiMn<sub>2</sub>O<sub>4</sub>-D are about 3–4 nm corresponding to the silica walls' dimensions

[31, 36]. As KIT-6 comprises two sets of interpenetrating mesopores which are interconnected by micropores [37], the growth of LiMn<sub>2</sub>O<sub>4</sub> within the both sets of pores of KIT-6 allows mesoporous LiMn<sub>2</sub>O<sub>4</sub> to be obtained with wall thickness equivalent to the size of the KIT-6 mesopores (5–8 nm) and a pore diameter equivalent to the KIT-6 wall thickness (3–4 nm) [31, 38].

After the chemical delithiation of LiMn<sub>2</sub>O<sub>4</sub>-C and LiMn<sub>2</sub>O<sub>4</sub>-D which forms  $\lambda$ -MnO<sub>2</sub>-C and  $\lambda$ -MnO<sub>2</sub>-D, the pore sizes increase to around 5 and 4–7 nm for the samples prepared with the concentrated and diluted precursor solutions, respectively, as shown in Fig. 4a, b. Both pore volume and surface area are increasing after delithiation. This enhancement is induced by the extraction of the lithium ions from spinel and the dissolution of manganese

**Table 1** Crystallographic and textural properties of commercial and synthesized materials

Material	Crystallographic characteristics			Textural characteristics	
	$d_{440}$ (Å)	$a$ (Å)	$L$ (nm)	$S_{\text{BET}}$ (m <sup>2</sup> g <sup>-1</sup> )	$V_t$ (cm <sup>3</sup> g <sup>-1</sup> )
LiMn <sub>2</sub> O <sub>4</sub>	1.461	8.266	35.6	3.5	0.003
$\lambda$ -MnO <sub>2</sub>	1.428	8.079	28	5.0	0.005
LiMn <sub>2</sub> O <sub>4</sub> -C	1.455	8.232	17.8	123	0.20
$\lambda$ -MnO <sub>2</sub> -C	1.420	8.034	17.1	152	0.28
LiMn <sub>2</sub> O <sub>4</sub> -D	1.444	8.166	19.4	78	0.12
$\lambda$ -MnO <sub>2</sub> -D	1.422	8.043	19.8	117	0.17

**Fig. 2** SEM pictures of **a**, **b** commercial LiMn<sub>2</sub>O<sub>4</sub>, **c** LiMn<sub>2</sub>O<sub>4</sub>-C, and **d** LiMn<sub>2</sub>O<sub>4</sub>-D

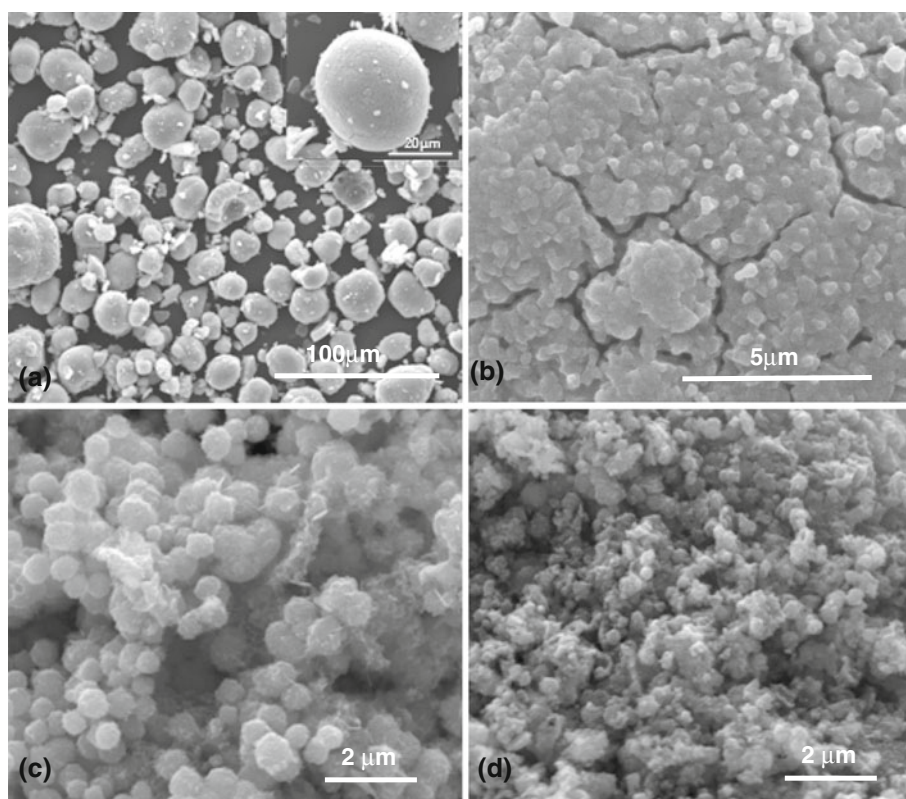
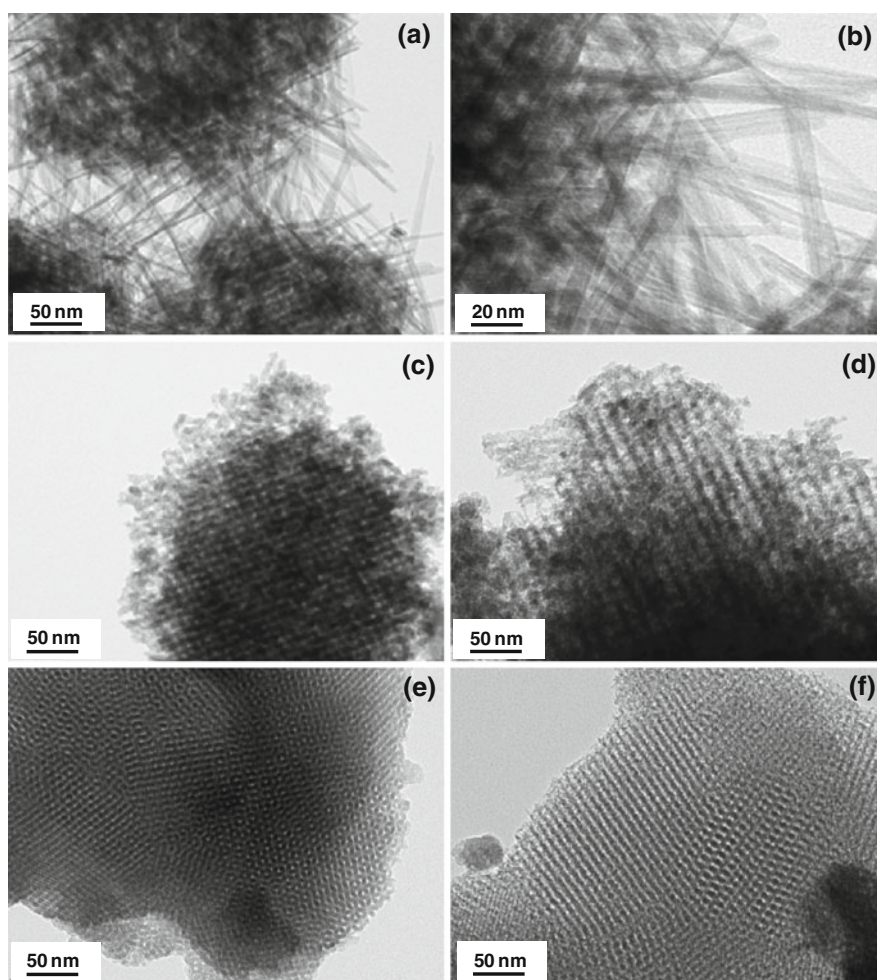


**Fig. 3** TEM images of **a, b**  $\lambda$ -MnO<sub>2</sub>-C **c, d**  $\lambda$ -MnO<sub>2</sub>-D and **e, f** KIT-6



ions during the acidic treatment. Hence, the manganese oxides with a better-developed porosity (152 and 117 m<sup>2</sup> g<sup>-1</sup> for  $\lambda$ -MnO<sub>2</sub>-C and  $\lambda$ -MnO<sub>2</sub>-D, respectively) are obtained.

By comparing the surface areas of the synthesized  $\lambda$ -MnO<sub>2</sub> materials with that of the commercially obtained sample, it is clear that the synthesis pathway is attractive in obtaining high surface area oxides exhibiting different morphologies beneficial for ion's transport in the electrochemical capacitor application.

Cyclic voltammetry and galvanostatic charge/discharge cycles at different current densities and impedance spectroscopy measurements were performed in two electrodes cell using a 1 M Li<sub>2</sub>SO<sub>4</sub> electrolyte to estimate the electrochemical properties. These investigations were focused on possible improvements, especially at higher current rates, with respect to a sample obtained from a commercial LiMn<sub>2</sub>O<sub>4</sub>.

The cyclic voltammograms for all  $\lambda$ -MnO<sub>2</sub> samples are presented in Fig. 5, while the calculated values of specific

capacitance from these curves are listed in Table 2. Enhancement of capacitance can be observed for both templated oxides comparing to the  $\lambda$ -MnO<sub>2</sub> obtained from the commercial product. The capacitances determined at 10 mV s<sup>-1</sup> are of the order of 93 F g<sup>-1</sup> ( $\lambda$ -MnO<sub>2</sub>-C) and 104 F g<sup>-1</sup> ( $\lambda$ -MnO<sub>2</sub>-D), whereas under the same conditions, the capacitance value is 42 F g<sup>-1</sup> for commercial  $\lambda$ -MnO<sub>2</sub>-derived material. None of the curves exhibits a rectangular shape which is typical for a quick dynamic of charge propagation. Deviation from ideal shape indicates limited diffusion of ions and a certain resistance of electrode material. However, tendency toward a quadrangle can be observed for voltammogram of  $\lambda$ -MnO<sub>2</sub>-D. This can be attributed to the regular 3-D pore structure of this sample with interconnected pores, which replicates the structure of the porous KIT-6 that favors a faster transport of ions. As shown in Table 2, the  $\lambda$ -MnO<sub>2</sub>-C sample exhibits in general the highest values of specific capacitance. This can be related to several issues as will be explained later.

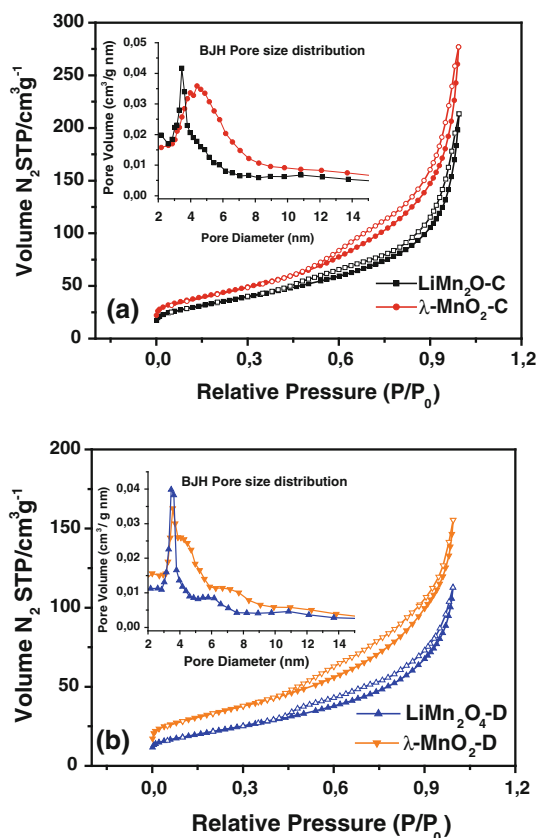


**Fig. 4** Nitrogen adsorption/desorption isotherm for **a** LiMn<sub>2</sub>O<sub>4</sub>-C and **b** LiMn<sub>2</sub>O<sub>4</sub>-D and their corresponding λ-MnO<sub>2</sub> and the BJH pore size distribution (*inset* of the figures)

If the values listed in Table 2 are only taken into account, then it could be assumed that the higher specific capacitance is related to the higher BET surface area and total porous volume of this material (Table 1). However, if the shape of the presented curves (Fig. 5) is analyzed, then the influence of the morphology has also to be considered. The nanowire or nanorod morphology of λ-MnO<sub>2</sub>-C provides a one-dimensional pathway for efficient electron transport, and facile ion migration in the electrode through the porous network formed by the tangled nanowires which can adapt to the volumetric changes easier during charge/discharge cycling [39].

In addition to the texture and morphology as mentioned above, the pseudocapacitive reactions are contributing to the capacitance. The voltammogram of λ-MnO<sub>2</sub>-C material is similar to the one registered for λ-MnO<sub>2</sub>, with a distinctive peak suggesting that the additional contribution to the capacitance is due to the pseudofaradic charge transfer reactions, in both cases. Because the structural framework of the initial spinel material is preserved, lithium-ion insertion/extraction into/out of the structure of λ-MnO<sub>2</sub> occurs in the Li<sub>2</sub>SO<sub>4</sub> aqueous solution during the charge/discharge, respectively [40]. The potential value of this

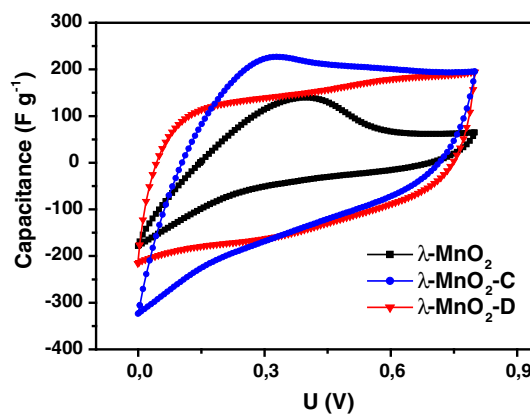
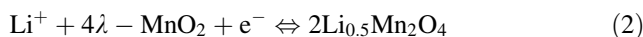


**Fig. 5** Cyclic voltammograms for λ-MnO<sub>2</sub>, λ-MnO<sub>2</sub>-C and λ-MnO<sub>2</sub>-D at a scan rate of 10 mV s<sup>-1</sup> in 1 mol L<sup>-1</sup> Li<sub>2</sub>SO<sub>4</sub> solution

peak (~0.3 V) correlates well with the thermodynamic Pourbaix data for the formation of Li<sub>0.5</sub>Mn<sub>2</sub>O<sub>4</sub> (Eq. 2) [41]:



On the contrary, in the case of λ-MnO<sub>2</sub>-D, this peak is no longer visible. A possible explanation for this behavior can derive from the structural differences of the LiMn<sub>2</sub>O<sub>4</sub> materials given the fact that their lattice parameters are different. From Table 2 it is noted that the lattice parameters of the commercial sample and sample C are much closer to the stoichiometric LiMn<sub>2</sub>O<sub>4</sub> than the sample D which is more toward the Li-substituted spinel (Li<sub>1+x</sub>Mn<sub>2-x</sub>O<sub>4</sub>) [42].

It is also known that more proton/Li<sup>+</sup> exchange happens with substituted spinels in acidic conditions because there were less Mn<sup>3+</sup> ions in these structures to allow for disproportionation reaction, and hence the obtained λ-MnO<sub>2</sub> possessed different structural features. The previously announced factors can be at the origin of the improved electrochemical performance of λ-MnO<sub>2</sub>-C.

Nevertheless, decrease of the capacitance with the increasing the scan rate is still observed for all samples (Table 2) even if the porosity and the diffusion were improved for the synthesized materials. This behavior was repeatedly observed for metal oxides [43, 44] and was explained by an ion-exchange mechanism [44]. The anions SO<sub>4</sub><sup>-</sup> require enough time to transfer from the solution to the surface of material to be intercalated/extracted into/out of material when charging/discharging, respectively. If the scan rate is low (1 mV s<sup>-1</sup>), the SO<sub>4</sub><sup>-</sup> have enough time to diffuse, and consequently more charge is transferred and stored than at a high scan rate. This explains the higher specific capacitance at low scan rate.

The results of galvanostatic cycling measurements at 100 mA g<sup>-1</sup> are presented in Fig. 6a. In the low current regime, λ-MnO<sub>2</sub> still exhibits high specific gravimetric capacitance, but the curve of λ-MnO<sub>2</sub> varies considerably from the symmetric triangle, which is typical for double-

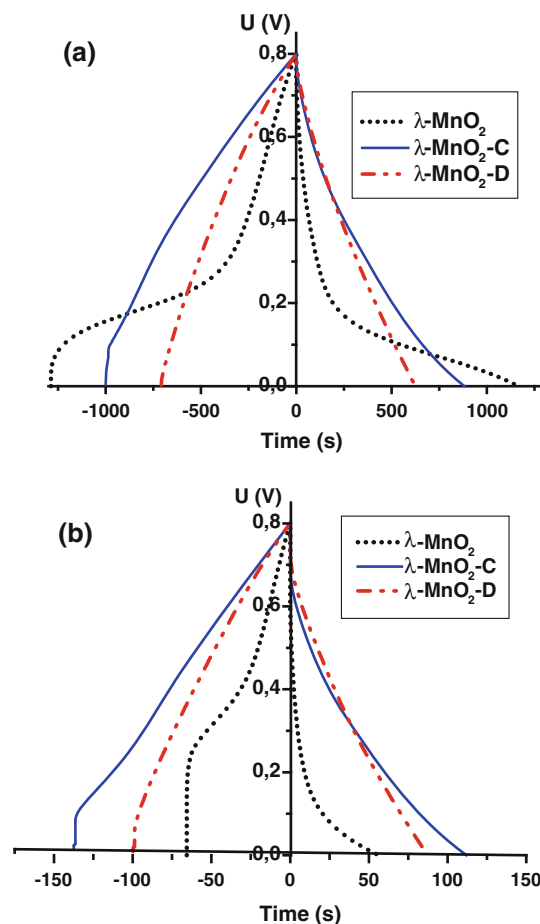
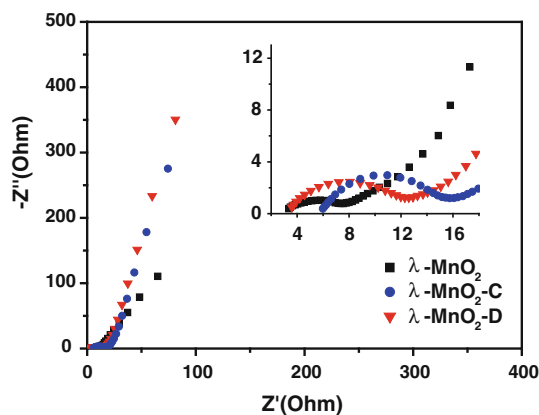


**Table 2** Specific capacitances ( $\text{F g}^{-1}$ ) estimated by three electrochemical methods for  $\lambda\text{-MnO}_2$ ,  $\lambda\text{-MnO}_2\text{-C}$ , and  $\lambda\text{-MnO}_2\text{-D}$ 

Method	Capacitance ( $\text{F g}^{-1}$ )		
	$\lambda\text{-MnO}_2$	$\lambda\text{-MnO}_2\text{-C}$	$\lambda\text{-MnO}_2\text{-D}$
Cyclic voltammetry at different scan rates ( $\text{mV s}^{-1}$ )			
1	193	283	195
2	106	200	159
5	65	139	129
10	42	93	104
20	25	54	75
100	5	8	22
Galvanostatic charging/discharging at different constant current ( $\text{A g}^{-1}$ )			
0.1	210	225	158
0.2	140	200	143
0.5	46	160	118
1.0	11	120	93
Impedance ( $1 \text{ mHz}$ )			
	309	171	137

layer charging electrode material. It must be mentioned that faradic reactions are involved during the cycling of the  $\lambda\text{-MnO}_2$  electrode with various oxidation states of manganese [6]. This is the reason for the nonideal shape of galvanostatic curves which are convex in shape instead of triangle, especially for the lower values of constant current. As the applied constant current is increased to  $500 \text{ mA g}^{-1}$ , the specific capacitance drops rapidly, which is clearly seen in Fig. 6b. The higher current density triggers a lower response of faradic reactions. However, both synthesized materials retain good capacitive properties (53–59 %) even at a higher current load ( $1 \text{ A g}^{-1}$ ) compared with the commercial material which is able to retain only 5 % of capacitance (Table 2). The charge and discharge curves are basically symmetric. What should be noticed is that the IR drop is diminished, and we should keep in mind that the  $\lambda\text{-MnO}_2\text{-D}$  possesses a 3-D structure that results in a more regular curve. The explanation can be attributed to the fact that porous texture facilitates the ions transport into the electrode and the more effective utilization of pseudocapacitive material. Moreover, an extended surface area is at the origin of increased double-layer capacitance. Hence, an improvement of about ten times of capacitance retention is obtained while using porous materials.

In order to compare the capacitive behavior of symmetric capacitors built from  $\lambda\text{-MnO}_2$  with three different structures, impedance spectroscopy measurements were performed in the frequency range from 100 kHz to 1 mHz. Results are presented in Fig. 7 in the form of Nyquist plot. Although the size of high-frequency semicircles is increased for both synthesized materials comparing with

**Fig. 6** Galvanostatic charge/discharge curves of symmetric capacitors for the  $\lambda\text{-MnO}_2$  electrodes at **a**  $0.1 \text{ A g}^{-1}$  and **b**  $0.5 \text{ A g}^{-1}$  in  $1 \text{ mol L}^{-1} \text{ Li}_2\text{SO}_4$  aqueous solution**Fig. 7** Comparison of Nyquist plots of  $\lambda\text{-MnO}_2$ ,  $\lambda\text{-MnO}_2\text{-C}$ , and  $\lambda\text{-MnO}_2\text{-D}$  electrodes

commercial one, the inclination of linear part is higher and tends to be vertical for materials with extended surface area. The results given by the impedance spectra suggest that the diffusion of lithium ions is facilitated as a result of



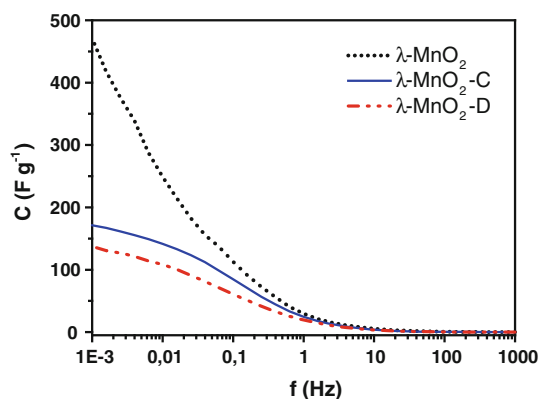


**Fig. 8** Capacitance versus frequency plot for the  $\lambda$ - $\text{MnO}_2$  electrodes of Fig. 7

the developed surface. The explanation for reduced conductivity may probably be attributed to the fact that the crystallinity is diminished.

In Fig. 8 a comparison of capacitance values with the frequency profiles of  $\lambda$ - $\text{MnO}_2$ ,  $\lambda$ - $\text{MnO}_2$ -C, and  $\lambda$ - $\text{MnO}_2$ -D is presented. This figure reveals that the capacitance at whole range of applied frequencies is higher for commercial  $\lambda$ - $\text{MnO}_2$ . The only improvement which has been obtained is moderate gradual falling of capacitance over a wider range of frequencies observed for templated materials rather than a rapid drop recorded for  $\lambda$ - $\text{MnO}_2$ .

## 4 Conclusions

A template approach is proposed in this study for the synthesis of a porous  $\lambda$ - $\text{MnO}_2$  with crystalline walls and an ordered interconnected pore structure. The physico-chemical investigations reveal that the morphology as well as the porosity of the resulting particles varies considerably depending on synthesis conditions. The material obtained by filling the silica with concentrated solution of precursors consists of entangled nanorods, whereas the second one (dilute solution) demonstrates the highly ordered 3-D cubic pore structure, replicating that of KIT-6 template. The surface area and pore volume is about 25 % larger for concentrated derived oxide compared with the diluted derived one. Consequently, the electrochemical performance of the prepared manganese oxides is largely affected by the textural properties and the morphologies of the particles. Both synthesized  $\lambda$ - $\text{MnO}_2$  materials exhibit better electrochemical performances in terms of specific capacitance and capacitance retention at high currents compared with the  $\lambda$ - $\text{MnO}_2$  material derived from the commercial sample because of the improved surface area and pore interconnectivity. In addition, the morphology of the  $\lambda$ - $\text{MnO}_2$ -C consisting of an open

mesoporous network formed by the entanglement of nanorods enabled enhanced electrochemical performance compared with the  $\lambda$ - $\text{MnO}_2$ -D. Nevertheless, a significant decrease of the capacitance with the increase of scanning rate still was observed.

This study demonstrates the synthesis of  $\lambda$ - $\text{MnO}_2$  architectures with high surface area and porous interconnected structure by a template approach as an effective strategy toward a new electrode material with improved performance for supercapacitors applications.

**Acknowledgments** The authors would like to thank Dr. Loïc Vidal and Stephan Knopf for the help provided during the TEM and SEM measurements. The authors thank Dr. Dan R. Simon for fruitful discussions. The CNRS (France) is also thanked for the financial support of the NANOCAP Project (PR3.2-9) through its energy program.

## References

- Kötz R, Carlen M (2000) Principles and applications of electrochemical capacitors. *Electrochim Acta* 45:2483–2498
- Etacheri V, Maram R, Elazari R, Salitra G, Aurbach D (2011) Challenges in the development of advanced Li-ion batteries: a review. *Energy Environ Sci* 4:3243–3262
- Xian H, Luo Z, Xie J (2012) Nanostructured  $\text{LiMn}_2\text{O}_4$  and their composites as high-performance cathodes for lithium-ion batteries. *Prog Nat Sci Mater Intern* 22:572–584
- Ragupathy P, Park D-H, Campet G, Vasan HN, Hwang S-J, Choy J-H, Munichandraiah N (2009) Remarkable capacity retention of nanostructured manganese oxide upon cycling as an electrode material for supercapacitor. *J Phys Chem C* 113:6303–6309
- Jayalakshmi M, Balasubramanian K (2008) Simple capacitors to supercapacitors: an overview. *Int J Electrochem Sci* 3:1196–2117
- Malak A, Fic K, Lota C, Vix-Guterl C, Frackowiak E (2010) Hybrid materials for supercapacitor application. *J Solid State Electrochem* 14:811–816
- Malak-Polaczyk A, Matei-Ghimbeu C, Vix-Guterl C, Frackowiak E (2010) Carbon/ $\lambda$ - $\text{MnO}_2$  composites for supercapacitor electrodes. *J Solid State Chem* 183:969–974
- Hunter JC (1981) Preparation of a new crystal form of manganese dioxide:  $\lambda$ - $\text{MnO}_2$ . *J Solid State Chem* 39:142–147
- Ammundsen B, Aitchison PB, Burns GR, Jones DJ, Rozière J (1997) Proton insertion and lithium-proton exchange in spinel lithium manganates. *Solid State Ion* 97:269–276
- Lee KT, Cho J (2011) Roles of nanosize in lithium reactive nanomaterials for lithium ion batteries. *Nano Today* 6:28–41
- Goodenough JB, Manthiram A, Wnetrzewski B (1993) Electrodes for lithium batteries. *J Power Sources* 43:269–275
- Tarascon JM, Guyomard PJ (1991) Li metal-free rechargeable batteries based on  $\text{Li}_{1-x}\text{Mn}_2\text{O}_4$  cathodes ( $0 \leq x \leq 1$ ) and carbon anodes. *J Electrochem Soc* 138:2864–2868
- Wohlfahrt-Mehrens M (2009) Secondary batteries -lithium rechargeable systems-lithium ion; Positive Electrode: Manganese Spinel Oxides. *Encyclopedia of Electrochemical Power Sources*. Elsevier, Amsterdam, The Netherlands, pp 318–327
- Thackeray MM, Johnson PJ, Depicciotto LA, Bruce PG, Goodenough J (2013) Electrochemical extraction of lithium from  $\text{LiMn}_2\text{O}_4$ . *Mater Res Bull* 19:179–187
- Horiba T, Hironaka K, Matsumura T, Kai T, Koseki M, Muranaka Y (2003) Manganese-based lithium batteries for hybrid electric vehicle applications. *J Power Sources* 119–121:893–896

16. Ma SB, Nam KW, Yoon WS, Yang XQ, Ahn KY, Oh KH, Kim KB (2007) A novel concept of hybrid capacitor based on manganese oxide materials. *Electrochem Commun* 9:2807–2811
17. Wang YG, Xia YY (2005) A new concept hybrid electrochemical supercapacitor: carbon/LiMn<sub>2</sub>O<sub>4</sub> aqueous system. *Electrochem Commun* 7:1138–1142
18. Kyotani T, Ma Z, Tomita A (2003) Template synthesis of novel porous carbons using various types of zeolites. *Carbon* 41:1451–1459
19. Rossinyol E, Arbiol J, Peiro F, Cornet A, Morante JR, Tian B, Bo T, Zhao D (2005) Nanostructured metal oxides synthesized by hard template method for gas sensing applications. *Sens Actuators Chem B* 109:57–63
20. Liu S, Yue B, Jiao K, Zhou Y, He H (2006) Template synthesis of one-dimensional nanostructured spinel zinc ferrite. *Mater Lett* 60:154–158
21. Vix-Guterl C, Saadallah S, Jurewicz K, Frackowiak E, Reda M, Permentier J, Patarin J, Béguin F (2004) Supercapacitor electrodes from new ordered porous carbon materials obtained by a templating procedure. *Mater Sci Eng B* 108:148–155
22. Kang M, Kim D, Yi SH, Han JU, Yie JE, Kim JM (2004) Preparation of stable mesoporous inorganic oxides via nano-replication technique. *Catal Today* 93–95:695–699
23. Lu A-H, Schuth F (2005) Nanocasting pathways to create ordered mesoporous solids. *C R Chimie* 8:609–620
24. Li WC, Lu A-H, Weidenthaler C, Schuth F (2004) Hard-templating pathway to create mesoporous magnesium oxide. *Chem Mater* 16:5676–5681
25. Schwickardi M, Johann T, Schmidt W, Schuth F (2002) High-surface-area oxides obtained by an activated carbon route. *Chem Mater* 14:3913–3919
26. Schuth F (2003) Endo- and exotemplating to create high-surface-area inorganic materials. *Angew Chem Int Ed* 42:3604–3622
27. Fuertes AB, Pico F, Rojo JM (2004) Influence of the pore structure on electric double-layer capacitance of template mesoporous carbons. *J Power Sources* 133:329–336
28. Jurewicz K, Vix-Guterl C, Frackowiak E, Saadallah S, Reda M, Permentier J, Patarin J, Béguin F (2004) Capacitance properties of ordered porous carbon materials prepared by a templating procedure. *J Phys Chem Solids* 65:287–293
29. Frackowiak E, Lota G, Machnikowski J, Vix-Guterl C, Béguin F (2006) Optimisation of supercapacitors using carbons with controlled nanotexture and nitrogen content. *Electrochim Acta* 51:2209–2214
30. Frackowiak E, Béguin F (2002) Electrochemical storage of energy in carbon nanotubes and nanostructured carbons. *Carbon* 40:1775–1787
31. Kleitz F, Choi SH, Ryoo R (2003) Cubic *1a3d* large mesoporous silica: synthesis and replication to platinum nanowires, carbon nanorods and carbon nanotubes. *Chem Commun* 17:2136–2137
32. Feng Q, Miyai Y, Kanoh H, Ooi K (1992) Lithium(1+) extraction/insertion with spinel-type lithium manganese oxides. Characterization of redox-type and ion-exchange-type sites. *Langmuir* 8:1861–1867
33. Patterson AL (1939) The Scherrer formula for X-ray particle size determination. *Phys Rev* 56:978–982
34. Shen W, Dong X, Zhu Y, Chen H, Shi J (2005) Mesoporous CeO<sub>2</sub> and CuO-loaded mesoporous CeO<sub>2</sub>: synthesis, characterization, and CO catalytic oxidation property. *Microporous Mesoporous Mater* 85:157–162
35. Sing SW, Everett DH, Haul R, Moscou L, Pierotti RA, Roquerol J, Siemieniewska T (1985) Reporting physisorption data for gas/solid systems with special reference to the determination of surface area and porosity. *Pure Appl Chem* 57:603–619
36. Parmentier J, Patarin J, Dentzer J, Vix-Guterl C (2002) Formation of SiC via carbothermal reduction of a carbon-containing mesoporous MCM-48 silica phase: a new route to produce high surface area SiC. *Ceram Int* 28:1–7
37. Kim TW, Kleitz F, Paul B, Ryoo R (2005) MCM-48-like large mesoporous silicas with tailored pore structure: facile synthesis domain in a ternary triblock copolymer-butanol-water system. *J Am Chem Soc* 127:7601–7610
38. Jiao F, Hill AH, Harrison A, Berko A, Chadwick AV, Bruce PG (2008) Synthesis of ordered mesoporous NiO with crystalline walls and a bimodal pore size distribution. *J Am Chem Soc* 130:5262–5266
39. Kim DK, Muralidharan P, Lee H-W, Ruffo R, Yang Y, Chan CK, Peng H, Huggins RA, Cui Y (2008) Spinel LiMn<sub>2</sub>O<sub>4</sub> nanorods as lithium ion battery cathodes. *Nano Lett* 8:3948–3952
40. Jayalakshmi M, Mohan Rao M, Scholz F (2003) Electrochemical behavior of solid lithium manganate (LiMn<sub>2</sub>O<sub>4</sub>) in aqueous neutral electrolyte solutions. *Langmuir* 19:8403–8408
41. Benedek R, Thackeray MM, van de Walle A (2010) Pourbaix-like phase diagram for lithium manganese spinels in acid. *J Mater Chem* 20:369–374
42. Masquelier C, Tabuchi M, Ado K, Kanno R, Kobayashi Y, Nakamura O, Goodenough JB (1996) Chemical and magnetic characterization of spinel materials in the LiMn<sub>2</sub>O<sub>4</sub>–Li<sub>2</sub>Mn<sub>4</sub>O<sub>9</sub>–Li<sub>4</sub>Mn<sub>5</sub>O<sub>12</sub> system. *J Solid State Chem* 123:255–266
43. Chen W, Rakhi RB, Hu L, Xie X, Cui Y, Alshareef N (2011) High-performance nanostructured supercapacitors on a sponge. *Nano Lett* 11:5165–5172
44. Panga H, Shia Y, Dua J, Maa Y, Li G, Chen J, Zhang J, Zheng H, Yuan B (2012) Porous nickel oxide microflowers synthesized by calcination of coordination microflowers and their applications as glutathione electrochemical sensor and supercapacitor. *Electrochim Acta* 85:256–262